Thermal Imaging for Defect Detection, Drying Dynamics, and Machine Learning-Based Mass Loading Estimation in Silicon Thin coating Production

Adil Amin[†], *Philipp Geiping*[†], *Ahammed Suhail Odungat, Fatih Özcan, and Doris Segets*[*]

Institute for Energy and Materials Processes – Particle Science and Technology (EMPI PST)

Carl-Benz-Straße 199, 47057 Duisburg, Germany

E-mail: doris.segets@uni-due.de

Doris Segets

Centre for Nanointegration Duisburg-Essen (CENIDE), University of Duisburg-Essen (UDE)

Carl-Benz-Straße 199, 47057 Duisburg, Germany

†These authors contributed equally to this manuscript

Abstract

This study demonstrates thermal imaging as a non-destructive, real-time quality control method for detecting coating defects, analyzing mass loading, and understanding drying dynamics in silicon-based thin coatings. Thermal imaging identifies critical defects such as streaks, pinholes, and chatter marks through distinct thermal signatures, with streaks reducing surface temperature by up to 15 °C. It establishes strong correlations between surface temperature, mass loading, and coating thickness; for instance, a 100 µm wet film thickness shows a surface temperature of ~50 °C, corresponding to a mass loading of 2.4 mg cm^{-2}. Drying dynamics reveal that thicker coatings retain more solvent, prolong drying, and shrink significantly, with 100 µm wet-gap coatings shrinking by up to 60%. A Random Forest machine learning model predicts mass loading with high accuracy (±0.3 mg cm^{-2}) using surface temperature data, highlighting the feasibility of thermal imaging-based quality estimation. While validated in a batch process, this approach is well-suited for integration into roll-to-roll production across diverse thin coating applications, such as batteries, solar cells, and functional films. Thermal imaging provides a robust pathway for real-time defect detection, drying optimization, and quality control, improving coating performance and production reliability.

Keywords

Thermal imaging, Machine learning, Defect detection, Non-destructive testing, Drying dynamics, Process monitoring in electrode production, Silicon-based thin coatings

1. Introduction

The rapid growth in the production capacity of lithium-ion batteries (LIBs) is driven by the global transition to renewable energy and the increasing demand for electric vehicles.[1] However, this surge in demand highlights the urgent need for innovative quality control methods to ensure the reliability and efficiency of these batteries.[2] At the core of the final LIB performance is the uniformity and quality of electrode coatings, which directly affect the battery's capacity, longevity, and safety.[3]

Although significant advancements have been made in active material development for LIBs, achieving consistent electrode coatings remains a challenge.[4] Defects such as uneven material distribution, agglomerates accumulation, pinholes, streaks, or variations in thickness can compromise battery performance, leading to reduced cycling stability or premature failure.[5, 6] Technologies based on radiation have gained significant attention for material characterization, offering non-destructive insights into thermal and structural properties. For instance, Neuhöfer et al.[7] demonstrated the utility of radiative heat transport analysis in porous silica materials, showcasing its potential to reveal critical thermal behaviors. Similarly, in this study, we explore how thermal imaging, a radiation-based technique, can provide valuable information about coating defects, mass loading, and drying dynamics in silicon-based thin electrodes. In addition to defects in electrode coatings, which can significantly impact performance, mass loading and thickness are also critical factors that require stringent quality control. Variations in mass loading and coating thickness can lead to inconsistent specific capacity and rate capability, further affecting overall battery performance.[8] Therefore, in addition to monitoring for defects, it is essential to implement quality control measures that ensure precise mass loading and uniform thickness, to maintain the desired electrochemical properties and improve production reliability. This creates a need for precise, nondestructive testing (NDT) methods that can detect these issues early in the manufacturing process.[3, 9] Ideally, these NDT methods should be compatible with roll-to-roll processing, allowing for real-time monitoring and correction of defects, mass loading, and coating thickness variations to ensure consistent electrode quality throughout production.

Thermal imaging may present a promising solution for addressing this challenge. It works by detecting the infrared radiation emitted by objects based on their temperature, allowing for the identification of temperature variations across the sample surface (in our

case the surface of the electrodes).[10] These variations may indicate the presence of defects or irregularities such as streaks, pinholes etc. In addition to defects in electrode coatings, which can significantly impact performance, detection of mass loading and thickness variations can also be explored using thermal imaging. Furthermore, thermal imaging can be used to monitor the dynamics during drying, as areas retaining moisture exhibit different thermal properties compared to fully dried regions. The ability of thermal imaging to detect subtle differences makes it ideal for ensuring coating quality without disrupting production processes.

In this study, we utilized thermal imaging in a batch process to analyse laboratory-scale thin coatings of silicon/carbon (Si/C) composite nanoparticles, beginning with its application for identifying and classifying three major defects—streaks, pinholes, and chatter marks—to demonstrate the method's potential for defect detection and quantification. We further expanded our investigation to assess variations in mass loading and coating thickness, highlighting how thermal imaging can capture these critical parameters. We also demonstrated the potential, as an initial proof of principle, to model the estimation of mass loading and coating thickness using surface temperature data of thermal images. Finally, we explored the drying process of the electrodes to understand its dynamic behavior. Together, our study reveals the capability of thermal imaging as an innovative approach to monitor essential parameters in LIB electrode manufacturing and potentially beyond.

2. Methods development

2.1. Materials

Si/C composite nanoparticles, produced via a gas-phase process as described elsewhere,[11] were selected for this thermal imaging study due to silicon's critical importance as a next-generation anode material in batteries and its role as an active material in solar cells. Si/C nanoparticles (Figure S1) were in the form of partly sintered aggregates, with primary particle sizes ranging from 100 to 250 nm and average aggregate sizes of approximately 550 nm.

2.2. Characterizations

The morphology and primary particle sizes of the Si/C active material were characterized using a JEM-2200FS (JEOL, Japan) transmission electron microscope, operating at an accelerating voltage of 200 kV. Surface temperature distribution across the coated electrodes was monitored using a TIMQVGA-HD O29 thermal imaging camera/IR-camera (Micro-Epsilon Messtechnik GmbH & Co. KG, Germany). Flatbed photo scanner (Cannon Scanner K10485, Vietnam) was used to capture high-resolution images of the dried coated layers, enabling visual inspection and comparison with thermal camera images. The mass of each electrode was determined using a high-precision analytical balance (KVD), and the coating thickness of the dried electrodes was measured with a digital micrometer screw gauge (Pollin Electronic Ladengeschäft, Germany).

2.3. Experimental and data processing

2.3.1. Slurry making, coating and drying protocol

Slurries with a total solid content of 30 wt.%, consisted of Si/C active material, carbon black, and polyacrylic acid in a solid mass ratio of 80:5:15. All slurries were prepared using a two-step dispersion process described in our previous work and in Supplementary Information (SI) (Figure S2).[12] The slurries were applied onto a 18 µm thick copper foil (Schlenk, Germany) using a blade coater (TQC Sheen, Industrial Physics, Netherlands) at a coating speed of 10 mm s^{-1}. The wet coating thickness was controlled by adjusting the doctor blade gap, called wet-gap height, according to the protocol explained in Section

3.1.4. For the analysis of as-prepared electrodes, the coated electrodes were dried in an oven at 80 °C for 1 hour under atmospheric pressure before they were transferred to the heated bed for thermal imaging.

2.3.2. Measurement set-up

To capture the surface temperature distribution of the coated electrodes, the thermal camera was positioned perpendicular to the sample, with an adjustable measuring distance of 12 cm to 40 cm (Figure 1). The detection temperature range was set from 20 °C to 100 °C, with an emissivity value of 0.9 for the coated surface, allowing for accurate detection of temperature variations. The TIM Connect software (Release 3.18.3103.0, Micro-Epsilon) was used for data acquisition, and temperature values were recorded as .csv files for further processing. The thermal data, saved as 382 × 288 matrices, was analyzed using MATLAB (version R2024b, License No. 40950020, provided by University of Duisburg-Essen). Each element in the matrix corresponds to the surface temperature of a pixel in the recorded image.

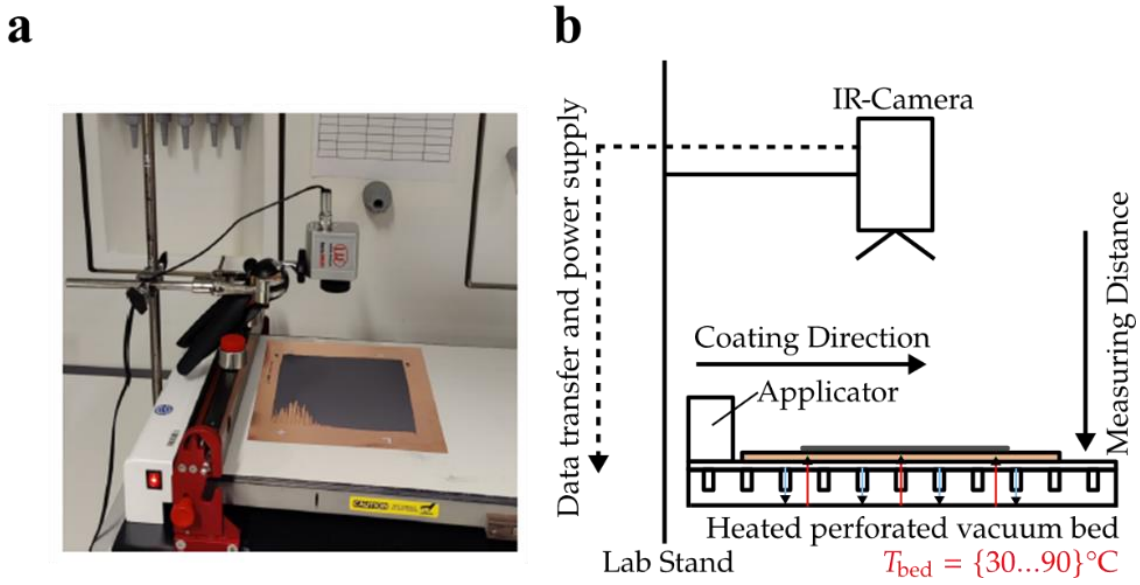

Figure 1. a) Photograph and b) schematic of the measuring setup, respectively.

2.3.2. Defects generation:

To generate the defects in our study, artificial model systems were developed. Streaks were created by scratching the wet coatings with a spatula, producing elongated marks parallel to the coating direction. Chatter defects, simulating vibrations, were generated by placing strips of adhesive tape under the copper foil (SI Figure S3), resulting in periodic lines due to rhythmic vibration of the doctor blade perpendicular to the coating direction. Pinholes were generated by air entrapment in the slurry during its preparation; the lid of the slurry mixing tube was left open while mixing at a high speed of 4000 RPM, allowing air to be dragged into the slurry. When this slurry was coated onto the copper substrate, air bubble bursting during drying led to pinhole defects. Creating these controlled, repeatable defects allowed us to validate the thermal camera's potential as a quality control tool when it is combined with image analysis. In the following paragraph, we will examine each defect type in detail.

2.3.3. Image processing

The information contained in thermal images, also called thermographs,[10] can be organized into a matrix with K rows and M columns:

$$T\,(x,y) = \begin{bmatrix} T_{11} & \cdots & T_{1M} \\ \vdots & \ddots & \vdots \\ T_{K1} & \cdots & T_{KM} \end{bmatrix} °C \qquad (1)$$

Each element in the matrix corresponds to a temperature value recorded as a single pixel by the thermal camera. A time-resolved series of thermal images of the same object can be viewed as a sequence of these matrices, T (x, y, t), where each matrix captures the temperature distribution across the object's surface at a specific time step. The image data is typically processed following the method illustrated in Scheme 1.

Scheme 1. Processing flow for thermal image analysis

The image processing techniques presented below will be applied to analyze coated anode layers, with the goal of identifying and classifying common coating defects and identifying mass loading/thickness variations in battery electrode fabrication.

Preprocessing: Once imported, the raw data was pre-processed to minimize noise and prepare it for further analysis. Various filters were applied based on the specific objective, such as noise reduction, edge detection, or enhancing image quality. The filters used included discrete approximations of Gaussian and median filters. The Gaussian filter, represented by a 3x3 kernel, was convolved with each pixel in the thermal image, effectively smoothing the data by reducing random noise.

$$F_{gauss}\,(x,y) = \frac{1}{16}\begin{bmatrix}1 & 2 & 1\\ 2 & 4 & 2\\ 1 & 2 & 1\end{bmatrix} \qquad (2)$$

Image segmentation: Image segmentation involves dividing an image into distinct regions, with thresholding being one of the simplest methods for this purpose. In thresholding, each pixel is evaluated against a set threshold value and assigned to a binary image. Pixels (px) with values below the threshold are given a value of zero, while those above it receive a value of one. In this work, thresholding was used to create masks that differentiate between regions containing the coating and areas displaying the copper substrate.

Feature extraction: Feature extraction refers to the transformation of data to emphasize specific image regions containing relevant characteristics. For defect detection, regions with temperature irregularities can be highlighted. One tool commonly used for this purpose is the Laplacian of Gaussian (LoG) filter. Here, the second derivatives were calculated in both image directions based on an image adjusted using the Gaussian filter.

$$F_{LoG}(x,y) = \Delta F_{gauss}(x,y) = \frac{\partial^2 F_{gauss}(x,y)}{\partial x^2} + \frac{\partial^2 F_{gauss}(x,y)}{\partial y^2} \qquad (3)$$

A discrete representation of this filter, in the form of a kernel, was convolved with the image on a pixel-by-pixel basis, particularly emphasizing areas with steep temperature gradients.

The second filter type used in this work was Dimensionality Filter for filtering Streak Defects based on their characteristic shape. Regions were classified as streaks if their length parallel to the coating direction was at least twice their elongation in the perpendicular direction. This ensured the effective differentiation of streak defects from other types of defects.

The third filter type used in this work was a Sobel filter. The Sobel filter is a type of edge-detection filter used to highlight regions of high intensity change in an image, effectively emphasizing edges. It works by calculating the gradient at each pixel, typically in horizontal or vertical directions, to detect boundaries or linear features. The Sobel filter is widely used in image processing to reveal structural details and enhance contrast along edges. In this work, a Sobel filter was applied to the thermal image data to emphasize vertical lines (chatter defect type). This filter calculated the gradient of image intensity at each pixel, highlighting vertical edges or temperature transitions. This approach proved useful in detecting linear features and boundaries within the images, enhancing the clarity of relevant structures for analysis.

Hit-and-Miss operation is a morphological operation used for refining feature extraction in binary images. It is a pattern-matching tool that refines feature detection by identifying specific shapes while ignoring others. In this context, it serves as a secondary filter to remove small, insignificant features that might have been highlighted by the Sobel filter but are not relevant to the analysis. This operation helps to focus on only the significant vertical features by filtering out minor noise or irrelevant details, thus refining the detection and making the results more accurate.

Classification: Once Regions of Interest (ROIs) were detected in the image, classification methods, including supervised and unsupervised approaches, were applied to categorize the regions based on different defect types. Specific geometrical constraints, such as aspect ratio and the alignment of the ROI relative to the coating direction, were used to assist in this classification.

Image registration: Image registration is a technique for aligning two images within a common coordinate system. It is especially useful when images have distortions, translations, or scale differences, such as those captured by different measurement

instruments. Although image registration is widely known and commonly used in fields like medical imaging, we developed a custom approach incorporating specific reference frames and code to achieve precise overlay by detecting distinct markers

In this work, we used the Maximally Stable Extremal Regions (MSER) algorithm to overlay thermal camera images with digital scans of dried layers. Coated layers were marked with symbols drawn with a white metallic lacquer pen, and 12 mm electrodes were then punched from these coatings for weighing and mass loading. After stamping, the coatings were digitally scanned using a flatbed scanner. These markers, visible in both thermal and scanned images, enabled accurate alignment. To precisely match surface temperatures from thermal images with the corresponding 12 mm punched electrode weights, the MSER algorithm was applied to extract the markings, ensuring accurate overlay of thermal images with scanned images.

2.3.4. Machine Learning-Random Forest Method

A Random Forest [13] is an ensemble learning method that constructs multiple decision trees using random subsets of the training data. Each tree is built by considering random subsets of features at each decision split, and predictions from each tree are aggregated (averaged for regression or majority voting for classification) to form the final prediction. In this study, we used the Random Forest Regressor from the scikit-learn [14] library (version 1.5.1) in Python to model the relationship between surface temperature and mass loading of electrodes. The scikit-learn library is designed for various machine learning tasks such as classification, regression, and clustering. The data was split into training and pre-testing sets (80 % for training and 20 % for pre-testing), and the model was trained using 100 decision trees. The model was saved using joblib for future use, enabling easy predictions on new data.

3. Applications

3.1. Defect detection in coated electrodes: Method application and analysis

As a first step, we introduced artificial defects, such as streaks, chatter, and pinholes, to demonstrate the effectiveness of thermal imaging in detecting these common flaws, which frequently arise during the coating stage. We chose to use artificial defects because they

provide consistency and control, enabling us to reliably simulate real-world conditions. Detecting these defects is critical due to their significant negative impact on the electrochemical performance of electrodes within cells and the additional safety risks they pose.

As previously mentioned, the detection of these defects is important during manufacturing as it can be detrimental for the performance of the electrode. For example, Mohanty et al.[5] studied the effect of electrode manufacturing defects in NMC532 cathodes on LIB performance. They found that agglomerates caused a rapid capacity fade, with only 12 % retention at 2C and 14 % at 5C after 200 cycles, compared to 70 % and 50 % for the baseline, respectively. Pinholes showed less severe capacity fading, retaining 47 % at 2C and 40 % at 5C. Moreover, the defect consisting of three parallel streaks exhibited significantly worse performance, retaining only 7 % capacity. Additionally, electrodes consisting of one single streak defect performed better than electrodes with three streaks defects but still showed reduced capacity retention, holding 45 % after 200 cycles at 5C, compared to the value of 50 % that was exhibited by the baseline.

Figure 2a shows a digital scan image of the test coating captured using flatbed scanner for digital photos, while Figure 2b presents the thermal camera image detecting the streaks. In all the detected streaks, a reduction in the surface temperature from 40 °C down to 25 °C is visible. Furthermore, the streaks appear as valleys with higher temperatures on the edges which decrease inwards. The digital scan of coated layer shows how slurry has accumulated at the edges of the streak because of scraping with the spatula. However, certain regions in the thermal image could not be classified as streak defects (at coordinates: 50, 150 px; 125, 125 px; 125, 190 px; 175, 180 px; 200, 190 px; 275, 140 px; 275, 100 px, highlighted with white circles in Figure 2b). To calculate the total area comprising streak defects, a dimensionality filter was applied to the thermal image (Figure 2b). Regions not meeting the aspect ratio criterion—where the length parallel to the coating direction is at least twice the perpendicular elongation—were excluded. Only regions elongated along the coating direction (left to right) were considered, leveraging the characteristic geometry of streaks. In the example shown (Figure S4), 1.94 % of the total coating area was identified as streak defects.

Figure 2c shows a foto scan of the test coating and the isolated thermal image of the respective coating to show the detection of chatter defects by thermal imaging (Figure 2d). In thermal images, these defects appeared as periodic temperature variations across

the surface, that were detectable by using image segmentation techniques. In chatter defects, the temperature drops by 5 °C than the maximum temperature of smoothly coated areas. Chatter defects could be filtered solely by applying the Sobel filter to the thermal image data to highlight vertical lines, and a hit-and-miss operation further refined the detection by excluding small or insignificant features (Figure S5). In the shown test coating, a total of 2.38 % of the area is considered as chatter defects. This is particularly important as in contrast to streak defects, these types of defects are hard to detect by visible eye from scanned images.

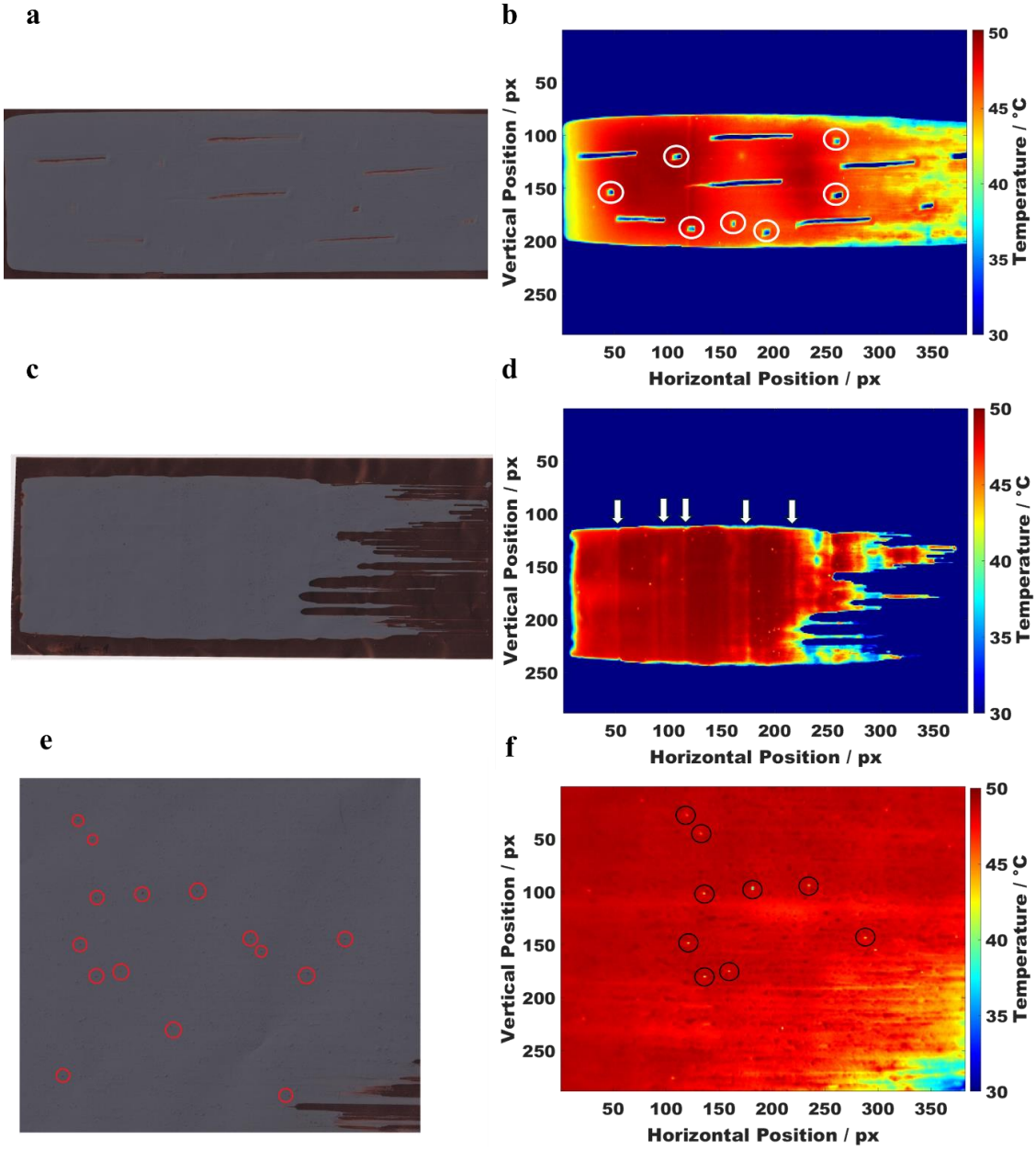

Figure 2. Foto Scans of test coatings showing defect types: a) streaks, c) chatter, and e) pinholes, respectively and corresponding thermal images: b) streak defects, d) chatter

defects (arrows indicate regions with 5 °C lower temperatures compared to adjacent smoothly coated areas), and f) pinhole defects, captured as a close-up from a 120 mm measuring distance.

Finally, Figure 2 e-f shows scan of the coated layer with pinhole defects and the corresponding thermal image of the layer. In the raw thermal image (Figure 2 f), small regions with lower temperature values (close to 40 °C) than the surrounding coating indicated the presence of pinholes. The largest pinhole defect, located at position (180, 100 px), occupied a measurable area of 4 × 4 px, making it detectable within the image. The automatic detection, processed through MATLAB, successfully filtered most of the pinhole defects, as shown in Figure S6. However, defects at horizontal positions ~140 px and ~290 px, which were visible in the scan, were not detected automatically. This limitation stemmed from the geometric filtering applied during detection. The filter checks the circularity of each region of interest (ROI), and due to the resolution limit of the thermal camera, defects were detected down to the level of single pixels. If the geometry of the ROI deviated from a circular shape, such as regions measuring 1 × 3 px, it was excluded from the pinhole classification. Overall, 0.00098 % of the total image area was identified as pinhole defects, highlighting the precision of the detection method. This quantification evidences the capability of thermal imaging for detecting even small-scale defects in coated electrodes, with room for refinement in addressing limitations related to resolution and geometric filtering.

Therefore, it can be stated that using image processing, various defect types were successfully detected and classified. However, a compromise was observed: moving the thermal camera closer improved the resolution for smaller defects like pinholes, agglomerates, and heat cracks, but made larger defects harder to detect. Close-ups also allowed the detection of additional defects, such as agglomerates (for example, at 150, 125 px; 75, 150 px) and shallow streaks (for example, 250, 180 px). Finally, it needs to be mentioned that in addition to pinhole defects, the thermal image (Figure 2f) revealed surface heterogeneity, with circular hotspots. These spots showing higher surface temperatures compared to the neighboring regions could indicate local variations in the active material and carbon black mixture, for instance due to agglomeration or inequal mass loading. This will be discussed in the following.

3.2. Mass loading and thickness variations

3.2.1. Sample coatings with wet-gap height gradients

As an initial approach to assess whether variations in mass loading and thickness can be detected using thermal imaging, model systems were coated with inclined blades to create controlled gradients of mass loading/thickness. To achieve these gradients, we adjusted the doctor blade by setting one side to a higher gap and the other to a lower gap, effectively controlling the wet-layer thickness across the coating. By controlling the wet-layer thickness in this way, we generated coatings with a gradual dry-thickness gradient after drying.

By preparing these coating samples using specific gradient wet-gap settings (100–20 µm, 100–40 µm, 100–90 µm, and a constant 100 µm wet-gap), we systematically examined how variations in coating thickness influenced the thermal response. Similar to the previous investigation of model defects, this setup allowed us to explore the sensitivity and limits of thermal imaging in detecting differences in mass loading and thickness, providing valuable insight into its effectiveness for assessing coating uniformity.

To ensure accuracy and reliability, temperature data were extracted from three equidistant line graphs (see Figure 3) across each of the four samples, including the constant 100 µm sample, with average values and standard deviations calculated for each. This statistical analysis across all samples quantifies temperature variations and identifies detectable thresholds for thickness and mass loading variations. Additionally, six electrodes were punched from three regions per sample to gather areal mass loading data (see method to calculate mass loading and thickness of the dry layer in SI heading 4.1.5) for comparison with the corresponding surface temperatures. This comparison is essential to validate whether temperature measurements can effectively represent the mass distribution, enabling us to further refine thermal imaging techniques for coating quality assessment.

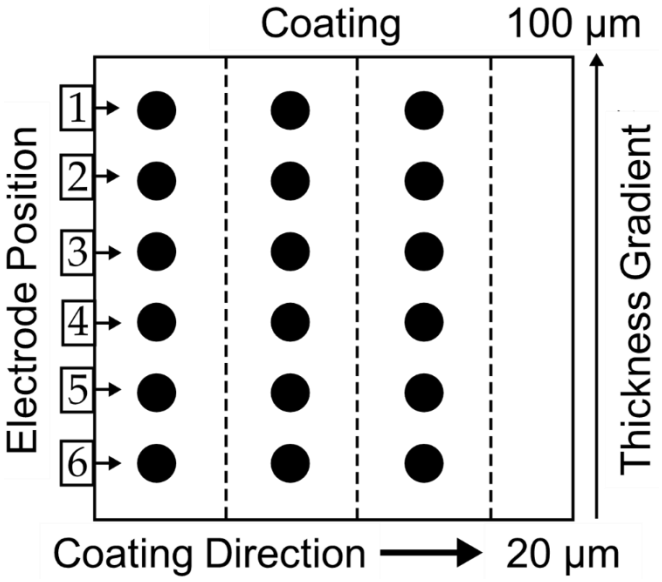

Figure 3. Positions of electrodes punched from samples coated with an inclined doctor blade. The coating is divided into three regions, each containing six electrodes punched perpendicular to the direction of coating.

Figure 4a shows the reference thermograph for a coating applied with a consistent doctor blade gap of 100–100 µm, set to achieve a wet-layer thickness of 100 µm along the length of the blade. This uniform gap setting results in minimal temperature variation across the surface. Although there was no gradient in the wet layer, slight temperature drops (color intensity change from dark red to red) were observed across the coated layer. Specifically, the temperature decreased by approximately 1–1.5 °C, with one side of the coated layer showing an average temperature of 50 °C (matching the set bed temperature) and the other side being 1–1.5 °C lower. This variation may be attributed to differences in mass loading or coating thickness, likely influenced by the rheological behavior of the nanoparticle-based slurry. In our previous publication [ref. will be inserted later], we demonstrated that nanoparticle slurries often result in coatings with uncontrolled mass loading and porosity/thickness. However, this study focuses solely on layer thickness and mass loading, not porosity. Thus, even with non-inclined blades, we expect slight variations in mass loading and dry layer thickness due to the intrinsic properties of nanoparticle-based slurries.

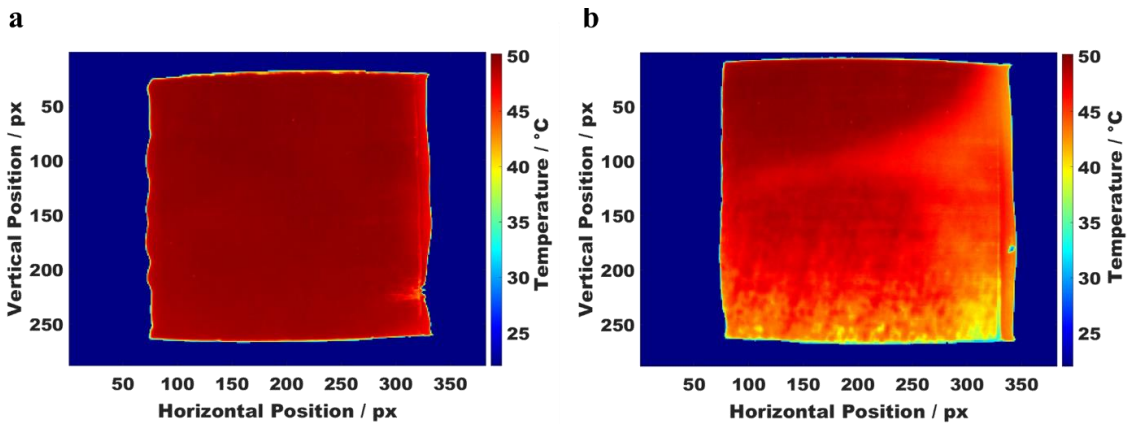

Figure 4. Thermal images of coatings prepared with different doctor blade wet-gap settings. (a) Reference thermograph with a consistent 100–100 µm blade wet-gap, showing minimal temperature variations across the surface. (b) Thermograph of a coating applied with an inclined blade setting of 100–20 µm, displaying a noticeable temperature gradient from top to bottom, as indicated by the color transition from dark red to yellow and green along the bottom boundary. The coating direction was from left to right.

In contrast, Figure 4b shows a thermograph of a coating prepared with an inclined doctor blade setting of 100–20 µm, resulting in a noticeable temperature gradient across the coated layer. This gradient is evident in the change in color intensity, shifting from dark red at the top (near the 100 µm setting) to light red and eventually to green toward the bottom (near the 20 µm setting). This color transition reflects the gradual decrease in surface temperature, with higher temperatures near the thicker regions and lower temperatures in the thinner areas. The temperature starts around 50 °C near the top, matching the set bed temperature, and gradually decreases to a minimum of approximately 42.5 °C at the bottom. This observed temperature gradient likely results from variations in coating thickness and mass loading caused by the inclined blade. The thicker sections near the 100 µm setting exhibit higher surface temperatures due to increased material mass, which emits more IR radiation. Conversely, the thinner areas near the 20 µm setting emit less IR radiation, resulting in lower detected surface temperatures.

These temperature variations highlight the sensitivity of thermal imaging in detecting subtle differences in coating thickness and mass distribution. This capability is particularly valuable for quality control in coatings that require uniformity in height and

mass loading. Additionally, for applications where coatings are designed with precise gradient specifications, thermal imaging enables accurate monitoring of spatial temperature variations associated with thickness and mass distribution.

To be more quantitative, Figure 5 summarizes the plotted relationship between specific gradient wet-gap height settings of the doctor blade (100–20 µm, 100–40 µm, 100–90 µm, and a constant 100 µm wet-gap) and two critical parameters: electrode mass loading and surface temperature of the corresponding coating across the coating width. The purpose of this figure is to examine how variations in wet-gap height influence these parameters, providing insight into the impact of the blade's inclination on the overall coating quality. From a quality control perspective, this figure shows how changes in mass loading due to blade inclination led to variations in the coating surface temperature, which are then captured using thermal imaging.

Specifically, Figure 5a plots the coatings surface temperature profile for each gradient wet-gap height setting. It can be seen from the figure that the coating’s surface temperature decreases where smaller wet-gap heights of blade were set. This plot is based on the average of three temperature line graphs along the width of coating at different positions of coating length (130, 220 and 250 px), with the filled area representing the standard deviation. Figure 5b, on the other hand, presents the measured electrode mass loadings (in mg cm^{-2}) at different blade inclinations along the coating, with the positions ranging from 100 µm on the left side of the blade to varied gap heights on the right.

As shown in Figure 5a, for all four samples, the surface temperature near the 100 µm gap height region of the doctor blade remained around 50 °C. It was observed that both surface temperature and electrode mass declined more sharply as the gap height gradient increased.

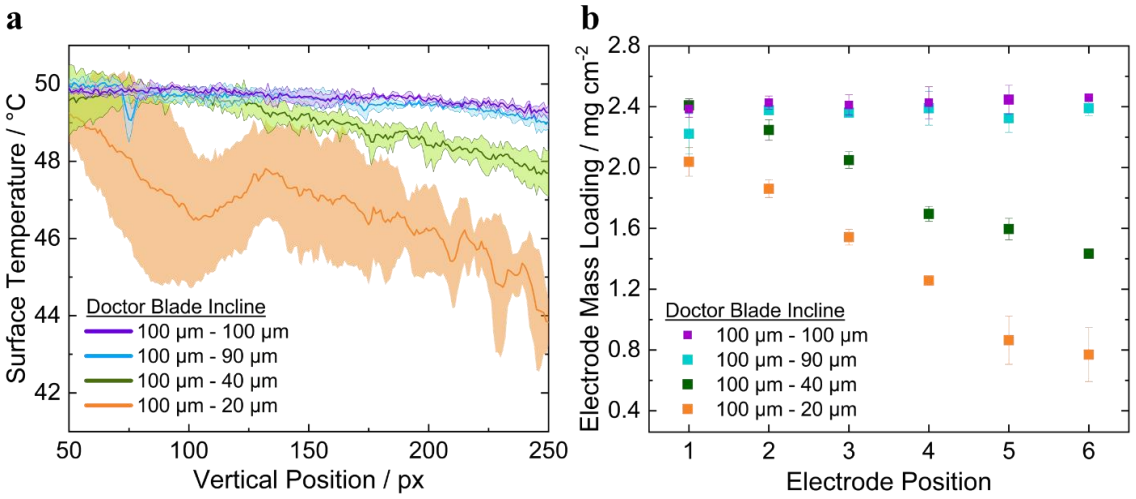

Figure 5a) Line graphs showing the temperature decrease with declining gap height of the blade. Three line-graphs were averaged, and the standard deviation is indicated by the filled area. b) Measured electrode mass loadings (mg cm^{-2}) at the vertical positions of the coating (with increasing position from the left side of the doctor blade set to 100 µm to the right side with varied gap height).

For the 100–20 µm gradient, the surface temperature decline reached 11 %, correlating with a 62 % reduction in electrode weight. Similarly, for the sample with a 100–40 µm gradient, the surface temperature dropped by 3.8 % corresponding to a reduction in mass loading by 40 %. The other samples displayed lesser declines in surface temperatures: 1.7 % for the sample with a 100–90 µm gradient and 1.2 % for the sample with a 100–100 µm gradient. These two samples, however, show a slight increase in electrode weight by 8 % and 3 %, respectively. The results reveal a strong correlation between surface temperature and mass loading, where steeper temperature gradients correspond to greater reductions in both temperature and mass.

This relationship can be applied during electrode manufacturing: a decrease in surface temperature signals a reduction in mass loaded onto the layer, while temperature variations across the surface indicate inconsistencies in mass loading. This highlights the potential for surface temperature analysis as an indirect indicator of mass loading, even detecting minor variations at low to middle mass loadings, making it a valuable tool for monitoring and ensuring consistent coating performance.

3.2.2. Coatings with fixed wet-gap heights

This chapter aims to investigate how fixed wet-gap settings of the doctor blade influence the mass loading of the coating, the dry layer thickness, and the corresponding surface temperatures of a coating, showing the correlations between these parameters. The ultimate objective is to develop an estimation model for mass loading based on surface temperature data, showcasing the potential of thermal imaging as a real-time quality control tool for detecting deviations in mass loading/thickness and for estimating mass loading in electrode fabrication. A fixed wet-gap height maintains a constant distance between the doctor blade and the substrate, ensuring consistent wet film thickness across the coating width. A mentioned, this uniformity is essential for applications requiring stable properties, such as battery electrodes, solar cells, and other thin-film technologies, where consistent thickness and material distribution are crucial for performance. Fixed wet-gap settings enable better control over coating properties like layer thickness, mass loading, and drying behavior, directly impacting product quality.

Different coatings with varying mass loadings/thicknesses were achieved by setting the doctor blade to fixed wet-gap heights of 20 µm, 40 µm, 60 µm, 80 µm, and 100 µm, resulting in a range of coating mass loadings/thicknesses. After following the drying protocol outlined in Section 2.3.1, thermal images of each coated layer were captured. For each wet-gap height setting, eighteen electrodes were punched from each sample, allowing for a detailed comparison of surface temperatures with electrode mass loading and thickness through image registration. Thermal images of the coated layers, marked with visible symbols, were overlaid with scanned images of the punched coatings using the maximally MSER algorithm. This technique enabled accurate matching of surface temperatures to the positions of the punched electrodes.

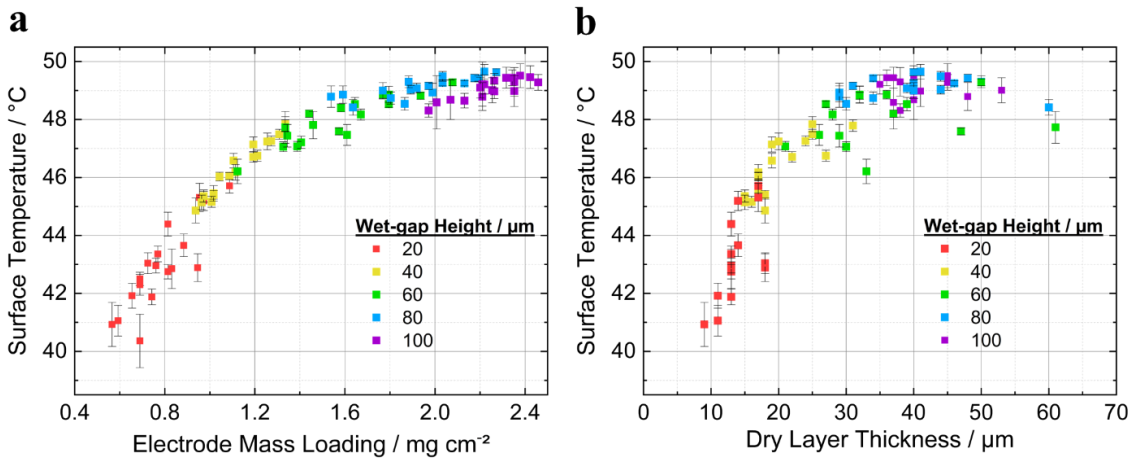

Figure 6. Dependence of the electrodes' average surface temperature on a) areal mass loading and b) dry layer thickness.

Figure 6a shows the surface temperature distribution across coatings produced with fixed wet-gap settings of 20, 40, 60, 80, and 100 µm. Despite the fixed settings, the final mass loading varied significantly. For instance, the 20 µm wet-gap resulted in mass loadings ranging from 0.56 to 0.94 mg cm^{-2}. Variability and standard deviation in mass loading decreased with higher wet-gap settings. For coatings produced at 100 µm, most electrodes exhibited mass loadings between 2.2 and 2.4 mg cm^{-2}, with a few as low as 2.0 mg cm^{-2}. This variability in mass loading, even at fixed wet-gap settings, can be attributed to the rheological properties of the nanoparticle slurry as mentioned before. Correspondingly, surface temperatures ranged from 40 °C for the low mass loadings to 49.5 °C for the high mass loading, further highlighting the relationship between mass loading and surface temperature. This increasing trend is in line with the data presented in Figure 5a, which further emphasizes the relationship between surface temperature and mass loading.

Detailed data analysis indicated a clear non-linear relationship between mass loading and surface temperature. At lower mass loadings, the surface temperature increased significantly with additional material (increase in mass loading), as captured by

the thermal imaging camera. However, as the mass loading continued to rise, the increase in surface temperature began to slow, resulting in a plateau around 2.0 mg cm^{-2}. This suggests a saturation effect, where further increase in mass loading results in diminishing returns on the finally measured temperature, i.e., sensitivity going down. This non-linear behavior highlights how, beyond a certain point, additional material does not produce a proportional increase in IR radiation, likely due to material properties that limit temperature increase at higher loadings and less likely the thermal camera limitations.

Figure 6b plots the relationship between the dry layer thickness of the coated electrodes and their average surface temperature. The thermal imaging analysis revealed a clear correlation, with surface temperatures increasing as the dry layer thickness increased. For coatings with a thickness of around 10 µm, the average surface temperature was approximately 40 °C, rising steadily to about 49.5 °C as the thickness reached 50 µm. However, beyond a dry layer thickness of around 45 µm, a saturation effect was observed, where further increases in the dry layer thickness resulted in minimal changes in the surface temperature. Additionally, the spread of thickness values varied depending on the set wet-gap, with the lowest standard deviation of ±3 µm (average around 13 µm) for a 20 µm wet-gap. The highest standard deviation of up to ~ ±10 µm was recorded for coating with a wet-gap set equal to or above 60 µm. This trend demonstrates a significant relationship between coating thickness and temperature, suggesting that thermal imaging can serve as a reliable indicator for process control of dry layer thickness.

Taken together, thermal imaging offers several strengths as a quality control tool in electrode fabrication. One of its key advantages is its ability to provide real-time, non-destructive measurements, allowing for continuous monitoring of coating parameters such as mass loading and dry layer thickness without interfering with the process. This makes it highly suitable for inline quality control, where rapid detection of deviations is essential. Additionally, the strong correlation between surface temperature and coating characteristics (such as mass loading and thickness) enables thermal imaging to serve as an effective indirect indicator of these properties, which can be challenging to measure directly in a production setting.

However, the results highlight some limitations of thermal imaging as well. While being effective for detecting larger variations in mass loading and thickness, its precision might diminish for small changes at high loadings or thicknesses due to saturation effects, where added material causes minimal temperature change. This saturation, however, is

material-dependent rather than a limitation of the technique itself. Despite this, thermal imaging remains a valuable tool for assessing coating quality and ensuring consistency.

In summary, this analysis demonstrates the potential of thermal imaging as a non-destructive tool with potential for real-time quality control in electrode fabrication. By correlating surface temperature with both layer thickness and mass loading, thermal imaging enables reliable monitoring of coating quality. Additionally, it provides a method for detecting defects, further enhancing quality control. Integrating this approach into production lines could significantly optimize electrode performance.

3.3. Mass Loading Prediction Using Thermal Imaging

3.3.1. Model development

This section investigates the potential to estimate mass loadings of Si/C composite electrodes using surface temperature data of the coating derived from thermal images. To explore the relationship between surface temperature and mass loading, we selected a combination of regression models and a machine learning approach. Traditional regression models—including piecewise, polynomial and logarithmic fits—were chosen for their simplicity and interpretability, making them ideal for capturing straightforward or segmented trends in the data.

Each regression model provides a different perspective on the temperature-to-mass-loading relationship, from linear segments to polynomial and logarithmic patterns. Therefore, in addition to regression models, we employed the random forest method, a machine learning technique well-suited for capturing complex, non-linear interactions within a given dataset. Random forest regression offers flexibility to model intricate patterns and detect subtle differences that traditional regression methods may overlook. We evaluated the accuracy of the models using R^2, Absolute Error, MAE, and RMSE. R^2 indicates the variance, the Absolute Error measures the raw difference between predicted and actual values, MAE measures the average error, and RMSE highlights larger errors. Together, these metrics offer a comprehensive view of the prediction reliability of each model and real-world applicability. Such way, this analysis helps to identify suitable predictive tools for monitoring mass loading in thin electrode coatings, potentially streamlining quality control and improving production efficiency.

Figure 7 shows the fitted graphs of different regression models applied to the mass loading (0.5 to 2.5 mg cm^{-2}) vs. surface temperature data, showing the relationship between mass loading and surface temperature.

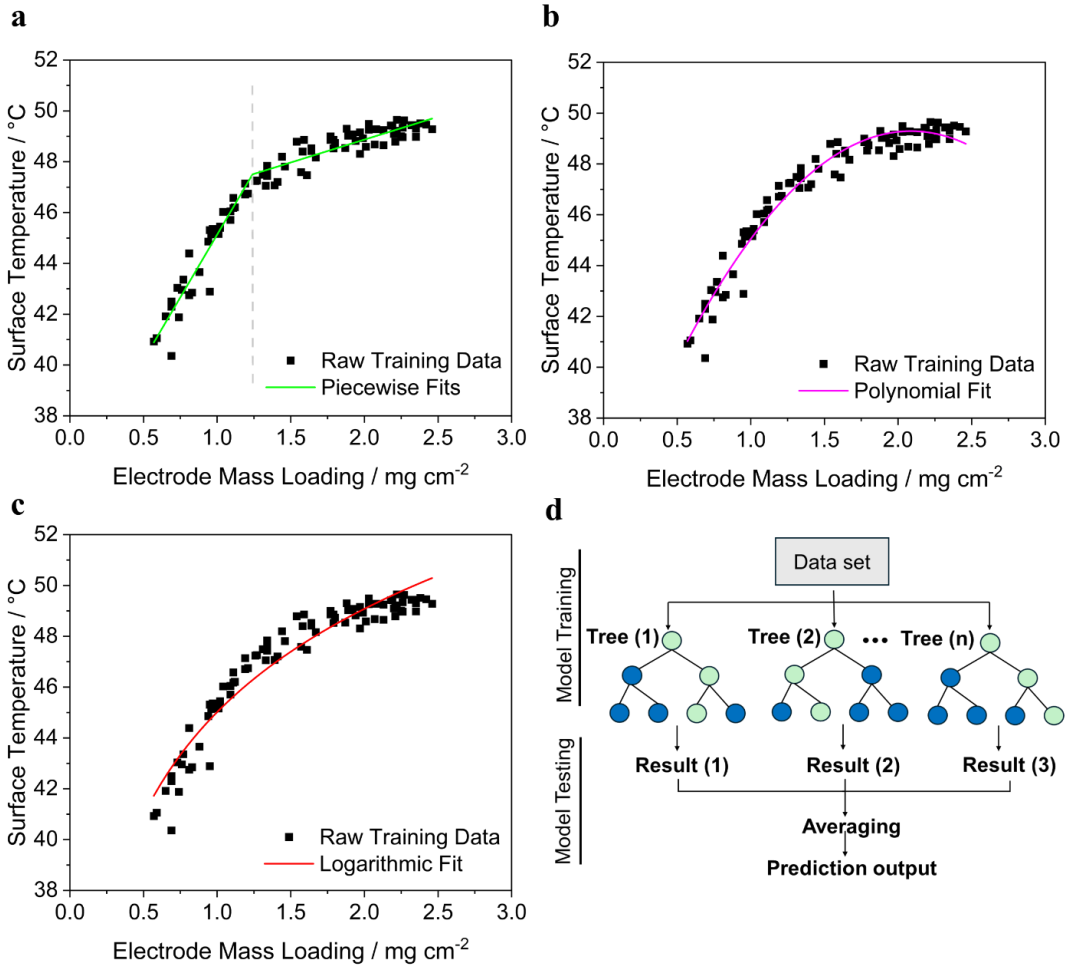

Figure 7. Model fits for electrode's mass loading (mg cm^{-2}) vs. its average surface temperature (°C): (a) Piecewise linear fit with a split at 1.23 mg cm^{-2}; (b) polynomial (degree 2) fit showing a peak trend; (c) logarithmic fit capturing temperature response to mass loading; (d) Random Forest process flow, highlighting ensemble prediction through multiple decision trees and result averaging.

Quantitative analysis using traditional regression models on this data yielded R^2 values of 0.90 and 0.76 for the two segments of the piecewise fit, and 0.96 and 0.92, for the polynomial and logarithmic fits, respectively. For applying the machine learning tool Random Forest, the dataset was divided into a training set and a test set. The data was split into training and pre-testing sets (80 % for training and 20 % for pre-testing), and

the model was trained using 100 decision trees, each built from random bootstrap samples of the data. The pre-test set was then used to assess the model's pre-performance, resulting in an R^2 score of approximately 0.94.

The fitted correlation equations for traditional models are shown as follows:

Piecewise fit

The fitted piecewise equation is as follows:

$$T_{surf}(m) = \begin{cases} a_1 m + b_1, & if\ m < m_{threshold}, \\ a_2 m + b_2, & if\ m \geq m_{threshold}, \end{cases} \quad °C \qquad (4)$$

For this relationship:

$a_1 = 2.3\ °C \cdot cm^2 mg^{-1}, b_1 = 15.7\ °C;$

$a_2 = 1.1\ °C \cdot cm^2 mg^{-1}, b_2 = 20.5\ °C;$

and $m_{threshold} = 1.23\ g\ cm^{-2}$

Polynomial fit

This model, with a parabolic form, captures the non-linear aspects of the data without segmenting it. The fitted equation is below:

$$T_{surf} = (-3.58\, m^2 + 14.98\, m + 33.65)\ \ °C \qquad (5)$$

Logarithmic fit

The logarithmic fit for the temperature vs. mass loading data is given by:

$$T_{surf} = (5.86\ \ln(m) + 45.02)\ \ °C \qquad (6)$$

With T_{surf} (°C) representing the average surface temperature and m (mg cm^{-2}) the mass loading of the electrode. The above equations (Equations 4-6) can be inverted to estimate the mass loadings of individual electrodes from the measured surface temperatures.

3.3.2. Model validation

Finally, we will validate the models and thereby compare them further with each other. To do so, new coatings were prepared at various wet-gap settings, from which randomly 36 individual electrodes were cut out, and their surface temperatures were taken from thermal images using MSER algorithm (see section 2.3.3. Image processing). Mass loadings for each electrode were then estimated using three traditional regression models—piecewise, polynomial, and logarithmic fits—developed above. Additionally, after training the Random Forest Regressor on training data (Figure 6a), these surface temperature measurements (from the new coating that was not part of the data shown so far) were input to predict mass loadings via the machine learning approach. The estimated mass loadings from each model were then compared to actual mass loadings obtained through direct measurement using a weighing technique.

Figure 8 presents a comparison between the actual mass loadings, measured by weighing, and the estimated mass loadings derived from surface temperature measurements using the three traditional regression models (piecewise, polynomial, and logarithmic fits) and the machine learning-based Random Forest Regressor.

Figure 8a shows the estimated results of the mass loadings from thermal data using piecewise linear model, with a comparison to the measured values. The results show that the piecewise linear model divides the estimated mass loadings data into two linear segments, estimated using one equation below a cutoff temperature of 47.3 °C (corresponding to a cut-off mass loading of 1.23 mg cm^{-2}) and another above it. This approach effectively estimates lower mass loadings using thermal data but struggles to capture the non-linear relationship, particularly at the curvature and for higher mass loadings in the mass loading vs. surface temperature correlation.

Figure 8b presents mass loading predictions using the polynomial model, comparing them with the measured values. The polynomial model shows an overall performance similar to the piecewise fit: it closely estimates lower mass loadings but struggles to capture the curved relationship at higher mass loadings. An additional limitation of the polynomial model is that at higher surface temperatures, the predictions for thicker electrodes became problematic due to the non-real solutions. This occurs because the polynomial model is solved using a quadratic equation, where imaginary solutions can arise under certain conditions. Therefore, this model does not even cover a full range of electrode mass loadings.

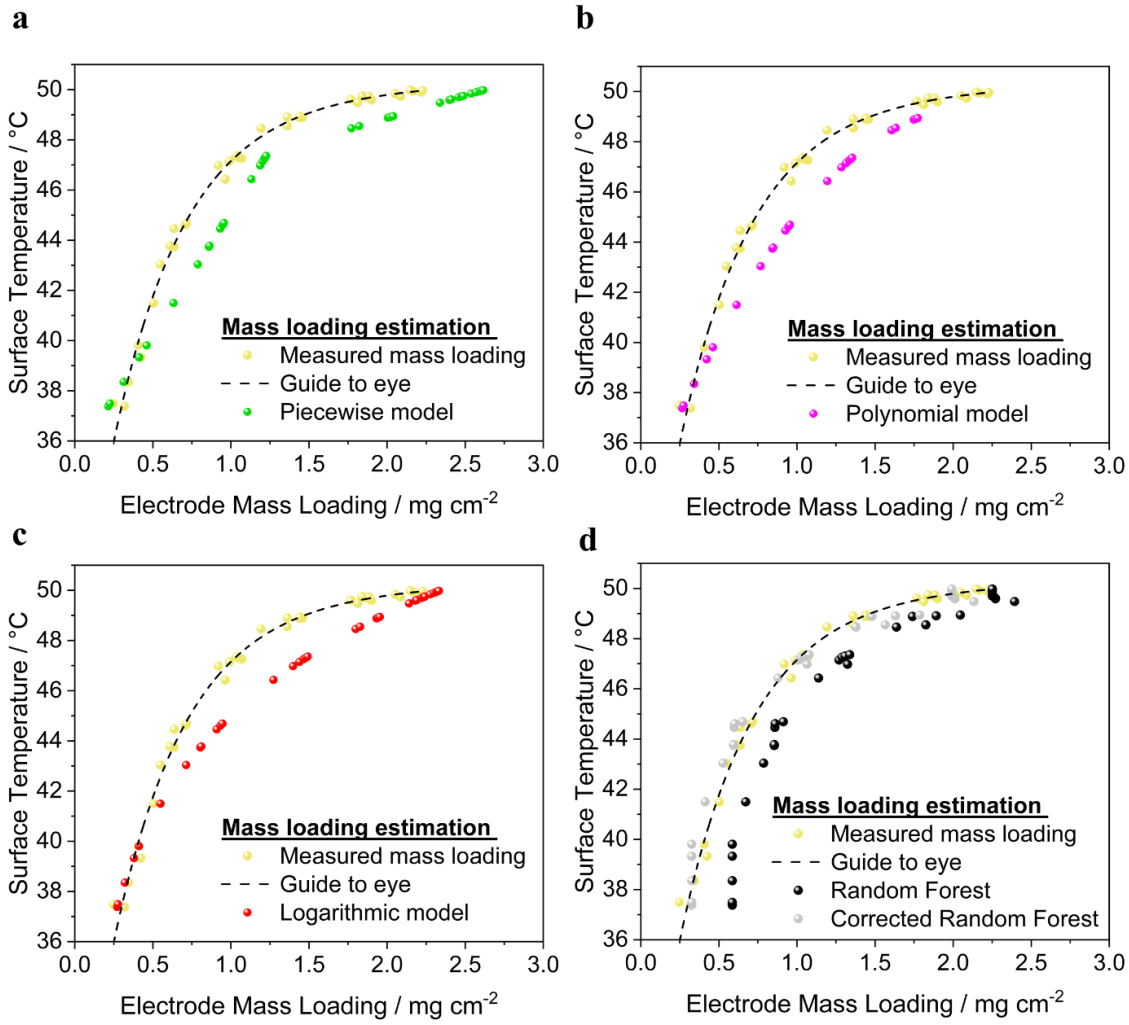

Figure 8. Comparison between actual mass loadings (measured by weighing) and estimated mass loadings derived from surface temperature measurements using four models: (a) piecewise model, (b) polynomial model, (c) logarithmic model, and (d) Random Forest method. Each subplot shows the model's performance in predicting the mass loading based on the surface temperature data.

In Figure 8c, the mass loading predictions based on surface temperatures using the logarithmic model are shown, with a comparison to the measured values. While logarithmic models are often effective for data trends that stabilize at high values, this model also predicted the mass loadings at extreme ends well. However, in curvature the prediction is very poor.

Finally, Figure 8d shows mass loading predictions for electrodes, derived from surface temperature data using the Random Forest Regressor, compared with the measured values. This machine learning model offers flexible estimations of the mass loading-temperature relationship, accurately modelling the curvature (dark spheres in Figure 8d). Initially, the machine learning model had difficulty in estimating very low mass loadings (lower surface temperatures) due to the absence of surface temperature data for mass loadings below 0.5 mg cm^{-2} in the training data set. This is in line with the expectation as machine learning models are known to get ineffective when they go out of the trained parameter space. Therefore, we added temperature data (6 electrodes) for mass loadings below 0.5 mg cm^{-2}. It significantly improved the model's performance (Figure S8) for estimating low mass loadings, highlighting its adaptability. Unlike conventional models, which require new equations with each update, the Random Forest Regressor can incorporate new data whenever they become available to continuously improve its predictions.

Furthermore, the Random Forest Regressor outperformed conventional models by better capturing the trend in the data. In an industrial setting, process parameters are typically controlled to maintain consistent product quality. Since the Random Forest Regressor's mass loading predictions exhibited homogeneous deviations, it allows for the application of correction factors to adjust the model's output, offering greater control over the process. Therefore, a constant correction factor of 0.26 mg cm^{-2} (which is the knowledge of error we obtained from pre-testing in the model development where R^2 was 0.94) was applied to data. As can be seen in grey data points, an excellent match of estimated and measured mass loadings was observed. Application of such correction factors is not possible for conventional models because they do not follow the exact trend in their estimations.

3.3.3. Error analysis

Figure 9 provides a comparative analysis of the absolute errors in mass loading predictions across different modelling approaches—conventional regression, random forest (trained at $m_{mass\ loadings}$ = 0.5-2.5 mg cm^{-2}), and corrected random forest—as a function of the electrode average surface temperature. Additionally, the MAE and RMSE for each model, including random forest flexible (trained at $m_{mass\ loadings}$ = 0.25-2.5 mg cm^{-2}) as a function of the electrode average surface temperature, along with the MAE

and RMSE for each model.

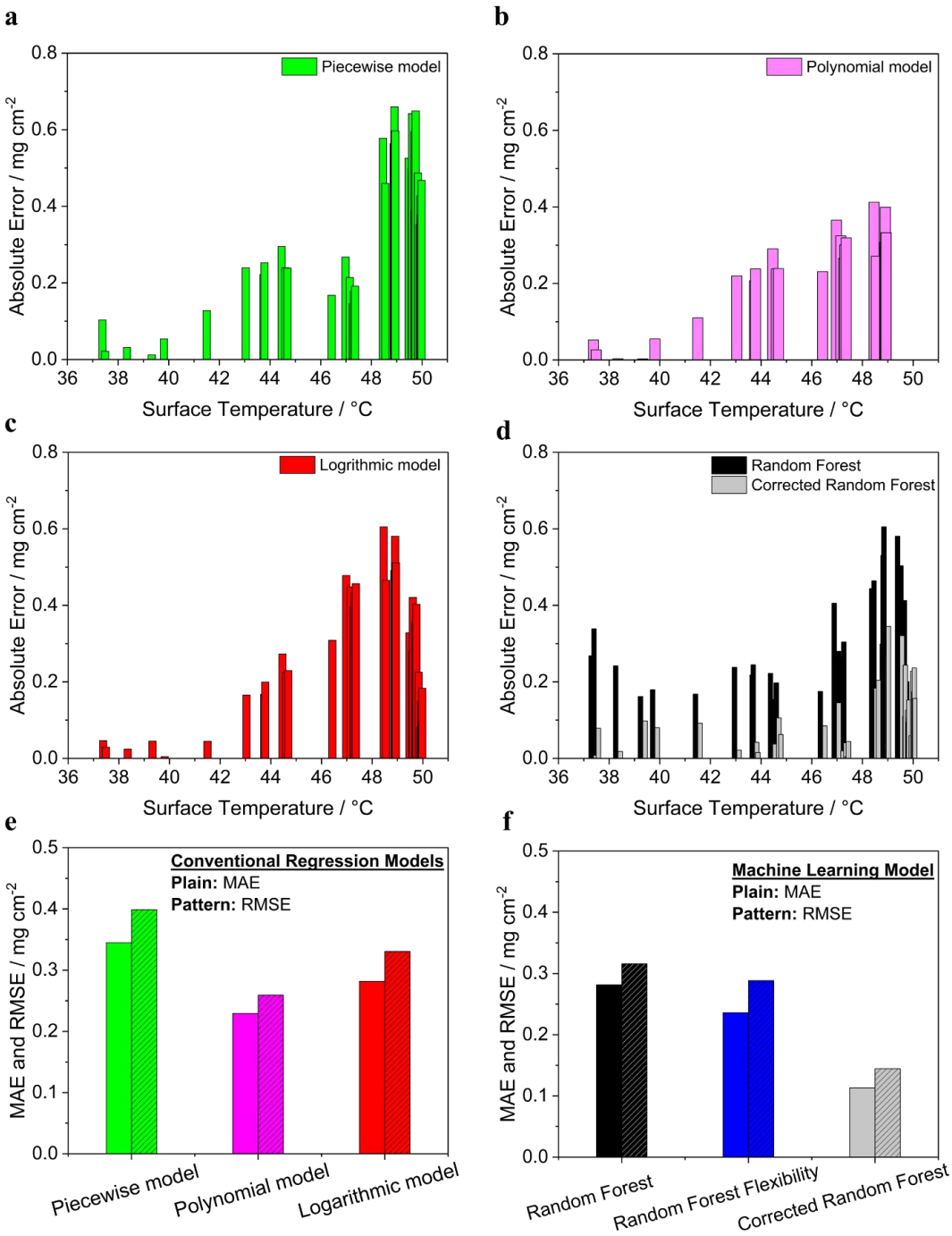

Figure 9. Comparison of absolute errors in the predicted mass loading across different regression and machine learning models as a function of electrode average surface temperature. a) Piecewise (green), b) polynomial (pink), c) logarithmic (red), and d) random forest (dark) and corrected random forest (grey) models. The bottom row presents

the MAE and RMSE for each model category, with results of the conventional regression models on the left and of the machine learning-based model on the right.

Figure 9a–d shows a comparative analysis of absolute errors in mass loading predictions across different models. The piecewise model performs well at low mass loadings (≤ 0.46 mg cm^{-2}) but shows increasing error, up to 0.65 mg cm^{-2}, at higher mass loadings due to a poor fit ($R^2 = 0.76$) in the second linear segment. The polynomial model accurately predicts lower mass loadings but becomes inconsistent at higher mass loadings and fails due to non-real solutions, limiting its applicability. The logarithmic model poorly aligns with the data, as it does not capture a plateau at higher temperatures, leading to discrepancies in predictions above 42 °C. In contrast, the Random Forest Regressor shows relatively lower absolute error at increasing mass loadings, as it better follows the curvature trend. Applying the correction factor further reduces the maximum mean absolute error from 0.60 to 0.35 mg cm^{-2} for estimation of the highest mass loading.

Figure 9e–f shows the MAE and RMSE values for various models used to predict the mass loading from electrode surface temperature. Among the conventional regression models, the piecewise model exhibited the highest deviations, with an MAE of 0.34 and an RMSE of 0.39, indicating its limited accuracy. The polynomial model showed improved performance, achieving an MAE of 0.23 and an RMSE of 0.25. The polynomial model provided a continuous equation for mass loading predictions and performed slightly better in predicting lower to mid-range mass loadings than the piecewise fit, but overall, it was less reliable due to its non-flexibility and inability to give any prediction about higher mass loadings. The logarithmic approach displayed moderate error levels, with an MAE of 0.29 and an RMSE of 0.33, placing it between the piecewise and polynomial models in accuracy. Again, the Random Forest Regressor demonstrated the lowest errors among the conventional regression models, with an MAE of 0.28 and an RMSE of 0.31, which were further reduced to 0.23 and 0.28, respectively, when temperature data in the very lower mass loading range (flexible random forest) was also included in the training of the model. Also as already seen above, the accuracy of the model improved significantly upon applying a correction factor, resulting in an MAE of 0.11 and an RMSE of 0.14 (Corrected Random Forest), the lowest error rates among all models evaluated in this study, highlighting its superior predictive capability.

In summary, the comparative analysis summarized in Figure 9 highlights the strengths and limitations of both conventional regression and machine learning models in predicting mass loading based on electrode surface temperature. While conventional regression models such as piecewise, polynomial, and logarithmic fits showed varying levels of accuracy, each had limitations, particularly at higher mass loadings or temperature ranges and their non-flexibility. The Random Forest Regressor outperformed these traditional approaches, with further improvements that could be achieved through correction factors that significantly reduced prediction errors. However, it is important to note that introducing correction factors adds an additional parameter to the model, which requires careful consideration and calibration for each processing material.

A potential limitation arises when the materials used in production undergo even slight changes, as model predictions are typically based on data from previously used materials. This challenge is particularly relevant in battery manufacturing, where small variations in formulation properties are common due to differences in the materials provided. Such changes could reduce the model's prediction accuracy unless it is updated with new data. This highlights the importance of using flexible machine learning models like Random Forest, which can effectively incorporate new datasets to adjust predictions to evolving material formulations or properties. By enabling continuous adaptation, these models ensure robust performance in dynamic environments where material variability is unavoidable. In this study, the Corrected Random Forest model demonstrated the best performance, delivering the lowest MAE and RMSE values and confirming its effectiveness for accurate mass loading estimation across a wide range of temperatures.

3.4. Investigation of time-dependent drying effects

Investigating drying curves is essential for optimizing both the drying process and the rate of movement in roll-to-roll (R2R) electrode manufacturing. The drying process significantly affects key electrode properties, including adhesion, rate capability, and capacity. Fast drying rates can cause defects like binder migration, leading to poor adhesion and uneven binder distribution.[15] In the R2R process, it is essential to carefully balance the coating speed with the drying rate. Typically, excessively fast line speeds can lead to incomplete drying and introduce defects, while slower speeds may enhance drying but reduce the overall production efficiency. Additionally, drying that is too slow or takes place at lower temperatures can destabilize the film, causing issues like de-wetting, further compromising the quality of the coating.[16] Therefore, understanding the drying behavior is crucial for achieving optimal coating quality and efficient production.

In this experiment, the thermal camera was positioned approximately 120 mm above the heated bed to capture accurate surface temperature measurements. Prior to slurry casting, the heated bed was pre-set to the target temperatures of 30 °C, 60 °C, and 90 °C. Coatings were applied with gap heights of 50 µm and 100 µm, and a fixed width of 60 mm. Surface temperatures of the coatings were recorded continuously over a period of 10 min. For the analysis, the recorded temperatures were averaged to assess the overall surface temperature profile of each coating condition. The shrinkage of electrode coatings during drying, as shown in Figure S9, was evaluated by comparing the wet-gap height with the final dry thickness. Coatings with a 100 µm wet-gap exhibited the highest shrinkage (60 %), while those with a 20 µm gap shrunk the lowest (31 %). This variation is likely due to differences in solvent evaporation rates in such a way that coatings with higher wet-gap settings retain more solvent initially, leading to greater shrinkage during drying.

Figure 10 shows the evolution of mean surface temperature over time for coatings with different initial wet film thicknesses at various drying temperatures, controlled by the heat-bed temperature. The camera was started before the coating was applied to the copper surface. The displayed temperatures are shown from the moment the applicator has fully coated the layer. This setup allows real-time observation of the drying behavior of coated electrodes, highlighting how solvent evaporates and how surface temperature changes during the drying process.

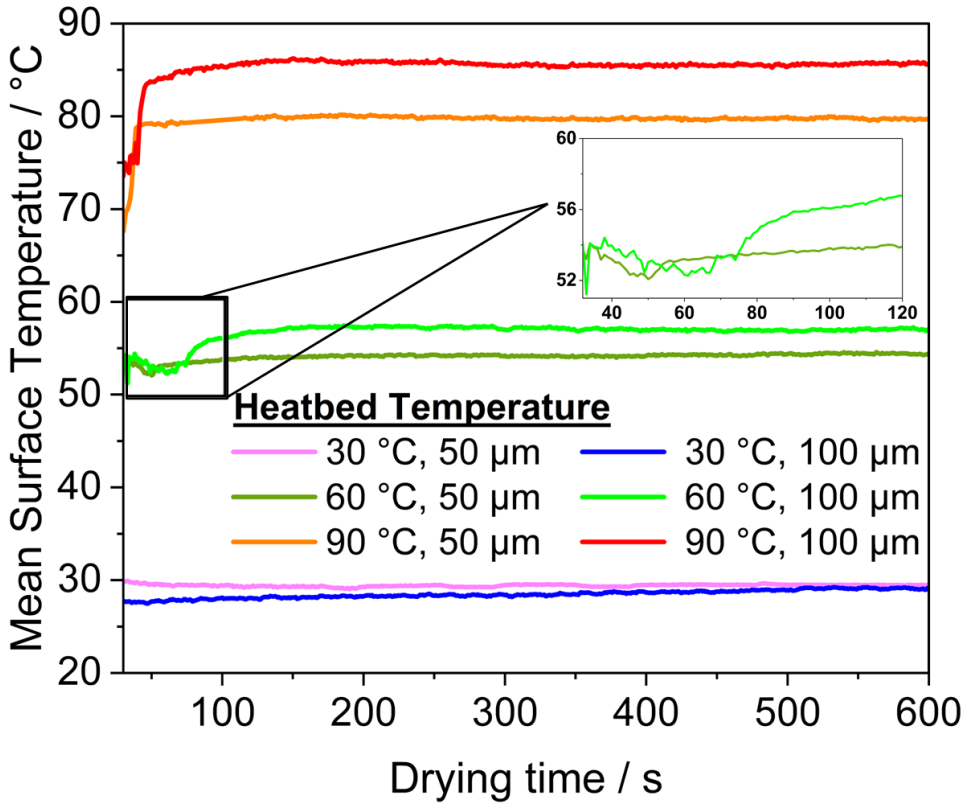

Figure 10. Evolution of mean surface temperature over time for coatings generated from varying initial wet film thicknesses (100 µm and 50 µm) at different heat-bed temperatures (90 °C, 60 °C, and 30 °C). The inset graph shows the fall and rise phases of the samples coated at a heat bed temperature of 60 °C.

The evolution of surface temperatures during drying is influenced by both the heat bed temperature and the wet-gap setting of the doctor blade. At a heat bed temperature of 90 °C, the surface temperature of the coating prepared with a wet-gap of 100 µm (resulting in a dry layer thickness of 40 µm) stabilizes at 85 °C, while the coating with a wet-gap of 50 µm (dry layer thickness of 20 µm) stabilizes at 80 °C within 150 seconds. At 60 °C, both coatings initially exhibit a temperature drop of approximately 2 °C within the first 15 seconds due to transient evaporation, followed by a gradual rise. The coating generated with a 50 µm wet-gap stabilizes at 54 °C after 10 seconds, whereas the coating generated with a 100 µm wet-gap stabilizes at 57 °C, requiring about 40 seconds to do so. At 30 °C, drying occurs predominantly through natural convection near room temperature, with minimal surface temperature variation.

The observations discussed above can also be visualized in a thermal video. For instance, Video S1 showcases sample coatings prepared with different wet-gap heights

(50 µm and 100 µm) using a doctor blade, with copper foil placed on a heat bed set to 60 °C. In Video S1a, for a wet-gap height of 50 µm, drying occurred almost instantaneously compared to the coating prepared at a 100 µm wet-gap height (Video S1b). In both samples, the reduction in surface temperature correlated with a visible drying front at the beginning of the process. As drying progressed, the solvent diminished into smaller islands, as seen in the thermal video. Once these islands disappeared, the surface temperature increased, indicating that the observed reduction in surface temperature was likely caused by the heat required for evaporation. However, the drying rates and overall drying times were noticeably different, with the 50 µm sample drying faster than the 100 µm sample.

These observations reveal how the wet-gap setting influences the drying process. Coatings prepared with larger wet-gap setting retain more solvent, requiring longer drying times due to the increased solvent content and slower diffusion of solvent to the surface. In contrast, coatings prepared with smaller wet-gaps dry faster because they contain less solvent, allowing for quicker diffusion and more efficient heat transfer. These differences are particularly pronounced at intermediate temperatures (60 °C), where transient evaporation and stabilization times differ significantly with coating thickness.

Overall, the heat bed temperature is the dominant factor in determining the drying speed. At higher temperatures (90 °C), drying progression stabilizes rapidly; at 60 °C, an intermediate stabilization occurs after an initial cooling phase; and at 30 °C, drying is slow and primarily driven by convection. However, the wet-gap height setting also plays a significant role, as coatings with higher wet-gaps require more time to dry and exhibit higher final surface temperatures due to prolonged evaporation processes.

4. Conclusions

This study successfully demonstrated the potential of thermal imaging as a non-destructive quality control tool for detecting coating defects and analyzing mass loading and thickness variations in the production of silicon-based thin coatings. Thermal imaging effectively identified critical defects such as streaks, pinholes, and chatter marks, with streaks reducing the surface temperature by up to 15 °C and chatter marks showing periodic variations of approximately 5 °C. These results highlight the method's exceptional sensitivity, surpassing traditional visual and laser-based inspection techniques in detecting subtle and performance-critical flaws.

Thermal imaging also revealed clear correlations between surface temperature, mass loading, and coating thickness. For instance, a 100 µm wet-gap coating exhibited a surface temperature of 49.5 °C and a mass loading of 2.4 mg cm^{-2}, whereas a 20 µm wet gap resulted in lower temperatures around 40 °C, corresponding to a mass loading of 0.6 mg cm^{-2}. Furthermore, integrating machine learning, particularly Random Forest models, enhanced the predictive capabilities of thermal imaging, offering superior accuracy in estimating mass loading compared to traditional regression approaches. These findings highlight the potential for thermal imaging to be incorporated into roll-to-roll processes for real-time monitoring and optimization.

Finally, the study examined drying dynamics and their dependence on heat bed temperature and wet-gap height. Coatings dried at 90 °C stabilized within 150 seconds, while drying at lower temperatures was slower and characterized by more gradual temperature increases. Drying dynamics also influenced the final electrode thickness, with coatings from a 100 µm wet-gap experiencing up to 60 % shrinkage during drying. These observations emphasize the importance of controlling both heat bed temperature and wet-gap height to achieve desired electrode properties.

In conclusion, the integration of thermal imaging into industrial-scale roll-to-roll production offers a promising pathway for real-time monitoring and correction of defects, mass loading, and thickness variations. This approach would enhance quality control, improve the mechanical and functional performance of coatings, and contribute to more reliable and efficient production processes. Moreover, it is also capable of providing kinetic inline or at-line data that could potentially be applied in future studies for validating numerical drying models.

Conflict of interest disclosure

The authors declare that they have no financial or non-financial competing interests to disclose

Data availability

The data that support the findings will be available in Zenodo

Acknowledgements

The authors gratefully acknowledge financial support from the Federal Ministry of Economic Affairs and Climate Action, Germany [Funding code 03EI3027A]. We also acknowledge the support of the Open Access Publication Fund of the University of Duisburg-Essen. We also thank Evonik Operations GmbH, Germany, for providing the Si/C powder used in this study.

References

[1] A. M. Ralls, K. Leong, J. Clayton, P. Fuelling, C. Mercer, V. Navarro, P. L. Menezes, *Materials (Basel, Switzerland).* **2023**, *16*.

[2] C. D. Reynolds, E. Kendrick, "Methodology in quality control for electrode processing", in *Processing and manufacturing of electrodes for lithium-ion batteries.* The Institute of Engineering and Technology, Stevenage. **2023**, p. 339 ff.

[3] A. Du Baret de Limé, T. Lein, S. Maletti, K. Schmal, S. Reuber, C. Heubner, A. Michaelis, *Batteries & Supercaps.* **2022**, *5*.

[4] B. Wu, J. Quinn, J. Li, Q. Li, D. Liu, W. Martin, K. Baar, L. Zhong, C. Wang, J. Xiao, *J. Electrochem. Soc.* **2024**, *171*, 50542.

[5] D. Mohanty, E. Hockaday, J. Li, D. K. Hensley, C. Daniel, D. L. Wood, *Journal of Power Sources.* **2016**, *312*, 70.

[6] A. Gyulai, W. Bauer, H. Ehrenberg. **2023**.

[7] A. M. Neuhöfer, K. Herrmann, F. Lebeda, T. Lauster, C. Kathmann, S.-A. Biehs, M. Retsch, *Adv Funct Materials.* **2022**, *32*.

[8] a) Y. Surace, F. Jeschull, P. Novák, S. Trabesinger, *J. Electrochem. Soc.* **2023**, *170*, 20510; b) P. A, S. S. Hegde, B. Ramachandra Bhat, C. Yadav K, S. Chakraborty, A. Ravikumar, S. D. George, Y. N. Sudhakar, R. Y, *Phys. Scr.* **2024**, *99*, 105922; c) P. Angelopoulou, G. Avgouropoulos, *Materials Research Bulletin.* **2019**, *119*, 110562; d) C. Yang, K. S. R. Chandran, *RSC advances.* **2023**, *13*, 3947;

[9] a) A. Benzaoui, D. Kocaefe, D. Bhattacharyay, Y. Kocaefe, *Metals.* **2017**, *7*, 128; b) A. Schoo, R. Moschner, J. Hülsmann, A. Kwade, *Batteries.* **2023**, *9*, 111; c) L. David, R. E. Ruther, D. Mohanty, H. M. Meyer, Y. Sheng, S. Kalnaus, C. Daniel, D. L. Wood, *Applied Energy.* **2018**, *231*, 446;

[10] M. Vollmer, K.-P. Möllmann, *Infrared Thermal Imaging: Fundamentals, Research and Applications*, 1st edition, Weinheim, Wiley-VCH. **2011**.

[11] H. Orthner, H. Wiggers, M. Loewenich, S. Kilian, S. Bade, J. Lyubina, *Journal of Alloys and Compounds.* **2021**, *870*, 159315.

[12] A. Amin, M. Loewenich, S. O. Kilian, T. Wassmer, S. Bade, J. Lyubina, H. Wiggers, F. Özcan, D. Segets, *J. Electrochem. Soc.* **2023**, *170*, 20523.

[13] B. Liu, M. Ma, J. Chang, Eds., *Information Computing and Applications: Third International Conference, ICICA 2012, Chengde, China, September 14-16, 2012. Proceedings*, Berlin, Heidelberg, Springer Berlin Heidelberg; Imprint; Springer. **2012**.

[14] Fabian Pedregosa, Gaël Varoquaux, Alexandre Gramfort, Vincent Michel, Bertrand Thirion, Olivier Grisel, Mathieu Blondel, Peter Prettenhofer, Ron Weiss, Vincent Dubourg, Jake Vanderplas, Alexandre Passos, David Cournapeau, Matthieu Brucher, Matthieu Perrot, Édouard Duchesnay, *Journal of Machine Learning Research.* **2011**, *12*, 2825.

[15] J. Kumberg, M. Baunach, J. C. Eser, A. Altvater, P. Scharfer, W. Schabel, *Energy Tech.* **2021**, *9*.

[16] a) L. Wengeler, *Coating and drying processes for functional films in polymer solar cells - from laboratory to pilot scale*, KIT Scientific Publishing. **2014**; b) M. Cakmak, G. Pearson, J. Greener, *Roll-to-Roll Manufacturing: Process Elements and Recent Advances*, Wiley. **2018**; c) J. Park, K. Shin, C. Lee, *Int. J. Precis. Eng. Manuf.* **2016**, *17*, 537;

Table of contents text

Thermal imaging provides a non-destructive, real-time quality control method for detecting defects, analyzing mass loading, and monitoring drying dynamics in silicon-based thin coatings. This study highlights its potential for diverse applications, enabling accurate defect detection, mass loading estimation using machine learning, and drying optimization, offering significant advancements in quality assurance for thin film technologies like batteries and solar cells.